Journal of Biomedical Optics

BiomedicalOptics.SPIEDigitalLibrary.org

Electron multiplying charge-coupled device-based fluorescence cross-correlation spectroscopy for blood velocimetry on zebrafish embryos

Paolo Pozzi
Laura Sironi
Laura D'Alfonso
Margaux Bouzin
Maddalena Collini
Giuseppe Chirico
Piersandro Pallavicini
Franco Cotelli
Efrem A. Foglia

SPIE.

Electron multiplying charge-coupled device-based fluorescence cross-correlation spectroscopy for blood velocimetry on zebrafish embryos

Paolo Pozzi,[a] Laura Sironi,[a] Laura D'Alfonso,[a] Margaux Bouzin,[a] Maddalena Collini,[a] Giuseppe Chirico,[a,*] Piersandro Pallavicini,[b] Franco Cotelli,[c] and Efrem A. Foglia[c]
[a]Università degli Studi di Milano-Bicocca, Dipartimento di Fisica, Piazza della Scienza 3, I-20126, Milano, Italy
[b]Università di Pavia, Dipartimento di Chimica, viale Taramelli, 12 – 27100 Pavia, Italy
[c]Università degli Studi di Milano, Dipartimento di Bioscienze, Via Celoria 26, I-20133, Milano, Italy

Abstract. Biomedical issues in vasculogenesis and cardiogenesis require methods to follow hemodynamics with high spatial (micrometers) and time (milliseconds) resolution. At the same time, we need to follow relevant morphogenetic processes on large fields of view. Fluorescence cross-correlation spectroscopy coupled to scanning or wide-field microscopy meets these needs but has limited flexibility in the excitation pattern. To overcome this limitation, we develop here a two-photon two-spots setup coupled to an all-reflective near-infrared (NIR) optimized scanning system and to an electron multiplying charge-coupled device. Two NIR laser spots are spaced at adjustable micron-size distances (1 to 50 μm) by means of a Twyman-Green interferometer and repeatedly scanned on the sample, allowing acquisition of information on flows at 4 ms–3 μm time-space resolution in parallel on an extended field of view. We analyze the effect of nonhomogeneous and variable flow on the cross-correlation function by numerical simulations and show exemplary application of this setup in studies of blood flow in zebrafish embryos *in vivo*. By coupling the interferometer with the scanning mirrors and by computing the cross-correlation function of fluorescent red blood cells, we are able to map speed patterns in embryos' vessels. [DOI: 10.1117/1.JBO.19.6.067007]

Keywords: fluorescence correlation; velocimetry; zebrafish; hemodynamics; microfluidics.

Paper 140181R received Mar. 20, 2014; revised manuscript received May 15, 2014; accepted for publication May 19, 2014; published online Jun. 20, 2014.

1 Introduction

Fluorescence correlation spectroscopy (FCS) is a well-established technique[1,2] and allows one to detect fluorescent particle motions from the fluorescence fluctuations. Fluorescently labeled molecules or cells passing through a tiny observation volume (essentially determined by the laser beam waist, ω_0, and excitation wavelength, λ) produce fluctuations whose typical decay time can be obtained from the autocorrelation function (ACF) of the emitted signal.

When the fluorescence signal is collected from a single excitation volume, the ACF is dominated by a hyperbolic decay that describes the translational diffusion through the volume. At very short times (<50 μs), exponential decays appear in the ACF due to chemical kinetics[2,3] or rotational diffusion.[4,5] A markedly different behavior appears when drift motions are present. An exponential decay, $\approx \exp[-(t/\tau_{VD})^2]$, contributes to the ACF and carries information on the drift speed modulus, $|\mathbf{V}|$, through the relaxation time $\tau_{VD} = \omega_0/|\mathbf{V}|$.[6–8] For situations in which both molecular diffusion and drift motions contribute to the fluorescence fluctuations, the ACF is characterized by two relaxation times: the diffusion and the drift times, τ_D and τ_{VD}. Their ratio depends linearly on the laser beam waist and the diffusion coefficient, D, as $\tau_D/\tau_{VD} \approx |\mathbf{V}|(\omega_0/D)$.

Single excitation volume ACFs have been used to map flow speed across circular[8] and square[9] cross-section microcapillaries. More complex flow patterns, such as vortexes in the middle of a T-junction of a microfluidic device[10] or *in vivo* studies of blood flow in zebrafish embryos,[11] have also been studied with this method. Diffusion coefficients and drift speeds can be simultaneously measured from single volume ACFs, although reliable parameters can be obtained only when the two relaxation times are approximately in the range of $1 < \tau_D/\tau_{VD} < 5$, as can be gained from numerical simulations.

A way to overcome this limitation is to cross-correlate the fluorescence signal coming from two laser foci set at a variable distance, $|\mathbf{R}|$, where $\mathbf{R}$ is the vector joining the two excitation volumes used in cross-correlation function (CCF) measurements.[12–14] In this case, in fact, the drift time is determined by $|\mathbf{R}|$ independent of the diffusion time and an appropriate choice of $|\mathbf{R}|$ in the experimental setup allows one to characterize both types of dynamics. Drift motions cause the appearance in the CCF of a quasi-Gaussian component whose maximum is a direct approximation of the drift time, as can be derived from numerical simulations. The computation of fluorescence CCF has been applied previously to study transport properties in a four-way junction in a microcapillary,[13] to solve issues related to the effect of laser beam distortion on the determination of the diffusion coefficients of fluorescent molecules,[15] and to map flow speed profiles.[16]

However, the application of cross-correlation analysis has been limited by the technical challenge to gather signals from different spatial locations on two separated light detectors.[13,14] Usually a fixed interspot distance is experimentally adopted.

*Address all correspondence to: Giuseppe Chirico, E-mail: Giuseppe.Chirico@mib.infn.it

0091-3286/2014/$25.00

This choice greatly reduces the possibility to investigate widely varying drift speeds and to map extended speed profiles in complex systems such as animal models *in vivo*. In these cases, it would be essential to develop methods for the parallel acquisition along the cross-section of the blood vessel.

The present report describes a cross-correlation spectroscopy setup that exploits an electron multiplying charge-coupled device (EM-CCD) camera to measure cross-correlation functions over extended fields of view. By coupling a Twyman-Green interferometer to the scanning head of an optical microscope we can collect, within a single CCD snapshot, an extended illumination pattern and measure cross-correlation functions over multiple points in parallel.

The outline of the paper is as follows. First, a theoretical background of auto- and cross-correlation experiments is given. We derive here analytical expressions and numerical simulations of cases that are experimentally relevant for the study of hemodynamics. The readers interested mostly in the experimental implementation of the setup and its validation can jump directly to the Results section. In a first part of the Results section, we report the validation experiments of the developed CCD-based cross-correlation spectrometer. These experiments are performed on borosilicate microcapillaries. In a second part of the Results section, we discuss the *in vivo* experiments on vessels of embryos of zebrafish (*Danio rerio*), a model organism widely used in developmental biology[17] and oncology.[18]

2 Theoretical Background

Theoretical analysis of ACF and CCF of the fluorescence emitted by single objects dragged in a flow have been presented previously.[13] We extend here this general treatment to cases that are relevant for the study of blood pulsation in an elastic vessel and that are, therefore, primarily related to speed inhomogeneity among cells and to periodic variations of the flow speed. To this purpose, we first briefly review the basic features of the ACF and CCF for drift motion and present numerical simulations of the correlation functions of flow regimes that are relevant in hemodynamics.

2.1 *Autocorrelation Function*

Fluorescence coming from a tiny volume ($\approx 1\ \mu m^3$) of a diluted suspension of objects at rest displays large fluctuations.[1,2] For simple three-dimensional Brownian diffusion, the ACF of the fluorescence fluctuations $\delta I(t) = I(t) - \langle I(t)\rangle$,

$$G(\tau) = \frac{\langle \delta I(t)\delta I(t+\tau)\rangle_t}{\langle I(t)\rangle_t^2}, \tag{1}$$

is a hyperbolic function [the parameter ξ is the excitation volume form factor (ratio of the size of the excitation volume along the optical axis with respect to the size in the focal plane)]:[19]

$$G_{\mathrm{Diff}}(\tau) = G(0)\frac{1}{1+\tau/\tau_D}\frac{1}{\sqrt{1+\xi^2\tau/\tau_D}}. \tag{2}$$

For confocal detection schemes, the diffusion time is related to the diffusion coefficient D and to the beam waist ω_0 as $\tau_D = (\omega_0^2/4D)$, and the volume form factor ξ is an experimental parameter, typically $\xi \cong 5$.[20] For two-photon excitation, the diffusion time is $\tau_D = (\omega_0^2/8D)$ and $\xi = \lambda/(\pi\omega_0)$, where λ is the excitation wavelength.[21] When the suspension is flowing at a speed $= |\mathbf{V}|$, the ACF is modulated by an exponential decay[6,7] whose relaxation is determined by the drift time, $\tau_{VD} = (\omega_0/|\mathbf{V}|)$, needed by the fluorophore to run through the excitation volume.

$$G_{\mathrm{drift}}(\tau;\tau_D,\tau_{VD}) = G_{\mathrm{Diff}}(\tau;\tau_D)\exp\left[-\left(\frac{\tau}{\tau_{VD}}\right)^2\frac{1}{\left(1+\frac{\tau}{\tau_D}\right)}\right] = G_{\mathrm{Diff}}(\tau;\tau_D)S(\tau;\tau_D,\tau_{VD}). \tag{3}$$

For single-spot ACF, the diffusion and drift times are linked by the laser beam waist and the drift speed as $\tau_{VD}/\tau_D \propto D/(|\mathbf{V}|\omega_0)$. For $\tau_D \geq \tau_{VD}$, the ACF is not markedly affected by the drift component. For microspheres 20 nm in size ($D \cong 10.7\times10^{-12}$ m^2/s, $\tau_D \approx 4.2$ ms) and a laser beam waist $\omega_0 \cong 0.6\ \mu$m, the minimum speed that can be reliably measured (corresponding to the condition $\tau_V \cong \tau_D$) is $|\mathbf{V}_{\min}| = (8D/\omega_0) \cong 140\ \mu$m/s. By simulating ACFs with added Gaussian noise (4%) and fitting them to Eq. (3), we estimate that the uncertainty of the diffusion and drift time is <2% and 7%, respectively.

Regarding *in vivo* applications, such as blood flows, particularly in the capillary bed at the vein-artery transition in small organisms[22] or complex vessel structures as those found in the hepatic microcirculation system,[23] a crucial limitation on the single-spot ACF is the lack of sensitivity to the direction of the drift motion of the single-spot setup. This limitation can be overcome when using a double-spot setup as discussed in the following section.

2.2 *CCD-Based Cross-Correlation Function*

In dual-spot setups, the flow parameters are measured from the cross-correlation $G_{X12}(\tau)$ of the signals $I_1(t)$ and $I_2(t)$, collected from two observation volumes spaced by the vector $\mathbf{R}$. We assume here that the two volumes lie along the flow lines (laminar flow with $\mathbf{R}||\mathbf{V}$). Equation (1) is then modified to a CCF of the type

$$G_{X12}(\tau) = \frac{\langle \delta I_1(t)\delta I_2(\tau+t)\rangle_t}{\langle I_1(t)\rangle_t\langle I_2(t)\rangle_t}. \tag{4}$$

For colloids with diffusion coefficient D and subject to a drift speed $|\mathbf{V}|$, the CCF results in a Gaussian modulation of the hyperbolic decay typical of the Brownian motion.[13]

$$G_{X12}(\tau;\tau_D,\tau_{VR}) = G_{\mathrm{Diff}}(\tau;\tau_D)\exp\left[-\frac{|\mathbf{R}|^2}{\omega_0^2}\frac{\left|1-\frac{\tau}{\tau_{VR}}\right|^2}{\left(1+\frac{\tau}{\tau_D}\right)}\right] = G_{\mathrm{Diff}}(\tau;\tau_D)S_R(\tau;\tau_D,\tau_{VR}). \tag{5}$$

The drift time is now the time needed by the colloids to cover the distance between the two observation volumes, $\tau_{VR} = |\mathbf{R}|/|\mathbf{V}|$, which is not coupled to the diffusion relaxation time, as is the case for the one-spot configuration. The CCF has a maximum that depends on the speed of the fluorophore and on the distance between the two observation volumes. As long as $|\mathbf{R}| \geq 2\omega_0$, at most a pseudo-correlation function decay [Eq. (2)] is present in the CCF due to the fluorescence leakage between the two observation volumes, but no maximum is found in the reverse CCF, $G_{X21}(\tau;\tau_D,\tau_{VR})$. The sensitivity of the direction of the drift motion of the CCF analysis can be, therefore, very high.

The lag time $\tau_{\max}$ of the maximum of the function $G_{X12}(\tau;\tau_D,\tau_{VR})$ is a good approximation of the drift time, $\tau_{VR}\approx|\mathbf{R}|/|\mathbf{V}|$, for large values of the diffusion time. The possibility to measure the flow speed directly from the maximum of CCF is very important for applications over extended samples. It is, therefore, useful to derive an analytical simple estimate of the discrepancy between the drift and the $\tau_{\max}$ times. We have then cast the relation between $\tau_{\max}$ and τ_{VR} as a universal dependence of the drift time accuracy δ_τ on the time ratio $\Gamma=\tau_{VD}/\tau_D$.

$$\delta_\tau=\sqrt{\left[1-\frac{(\tau_{\max}-\tau_{VR})}{\tau_D}\right]^2-1}=A_1\Gamma+A_2\Gamma^2, \tag{6}$$

where $\tau_{\max}$ is the lag time of the maximum of $G_{X12}(\tau;\tau_D,\tau_{VR})$.

For small values of the time ratio Γ, the parameter δ_τ is related to the difference between $\tau_{\max}$ and τ_{VR} as $\delta_\tau\cong\sqrt{2|(\tau_{\max}-\tau_{VR})/\tau_D|}$. Equation (6) represents a quasi-linear dependence of δ_τ on Γ ($A_1=0.95\pm0.04$ and $A_2=0.027\pm0.02$). For $\Gamma<0.1$ [equivalent to $|\mathbf{V}|>10(\omega_0/\tau_D)$], the lag time discrepancy is <0.5%, Therefore $(\tau_{\max}-\tau_{VR})<0.005\tau_D$. In the case of microbeads ($\tau_D\approx20$ ms, $\omega_0=0.8$ μm), the minimum speed for which $\tau_{\max}\approx\tau_{VR}$ is $|\mathbf{V}|\approx400$ μm/s. For blood red cells ($D\approx0.1$ to 0.2×10^{-12} m^2/s and $\tau_D\approx$ 500 ms), this conditions changes to $|\mathbf{V}|>16$ μm/s, which is typically met in the hemodynamics of small animal models.

The maximum of the correlation function can be matched to the acquisition time window of the EM-CCD (a lower bound of 4 ms up to ~1 s) by changing the value of the interspot distance $|\mathbf{R}|$. This distance should, however, be larger than ≈4 laser beam waists ($|\mathbf{R}|>4\omega_0\approx3$ to 4 μm) in order to avoid signal leakage between the two excitation spots.

Equation (6) agrees with that reported by Dittrich et al.,[13] but brings into evidence the universal character of the dependence of δ_τ on the time ratio Γ. A consequence of Eq. (6) is also that the difference between τ_{VR} and $\tau_{\max}$ increases when $\tau_{VR}\gg\tau_D$ since in this limit $\tau_{\max}\to0$ due to the rapid decay of the diffusion component, $G_{\mathrm{Diff}}(\tau;\tau_D)$, that dominates the CCF decay.

As for the case of the ACFs, we have performed an analysis of the accuracy and uncertainty on the best fit drift and diffusion times. The accuracy of these parameters is better than 2 to 3% even for 10% of added Gaussian noise for $1.3\geq\tau_V/\tau_D\geq0.5$, showing that these uncertainties are much better than those retrieved by the ACFs analysis.

2.3 *Cross-Correlation Function for Heterogenous and Time-Dependent Flows*

A straightforward application of two-spots cross-correlation studies is the measurement of blood flows in living organisms. Blood circulation is a periodic anharmonic process,[22] with a marked time variation (systole and diastole phases)[24] and space dependence along the blood vessels. Pathologies may add further heterogeneity. Moreover, the flow is often studied via the observation of blood cells, platelets, or microbeads that are discrete large objects sparsely distributed into the blood plasma. The measured CCF decay is then affected by reduced statistics and cannot be directly compared with the CCF decay predicted for a molecular solution.

Therefore, it is interesting to derive the functional form of the CCF for the cases in which sample heterogeneity and time dependence of the flow play a relevant role. We have selected three cases for which analytical or numerical analysis can be performed: the presence of multiple drift components, a distribution of drift speeds, and a harmonic time dependence of the flow. The first case is appropriate to describe CCF in a diluted suspension of large objects (here the red blood cells), through a superposition of a limited number of drift components (here only two for the sake of simplicity). The second case describes heterogeneity arising, for example, from vessel cross-sectional variation in time or severe pathologies. The third case is relevant for understanding the limit of CCF measurements for the measure of the systolic and diastolic flow speeds.

We first treat the effect of a drift speed distribution on the shape of CCF.

The distribution is assumed Gaussian in order to obtain analytical results.

$$P_V(|\mathbf{V}|;V_0,\sigma_V)=\frac{1}{\sqrt{2\pi}\sigma_V}\exp\left[-\frac{(|\mathbf{V}|-V_0)^2}{2\sigma_V^2}\right], \tag{7}$$

where V_0 is the maximum value of the speed distribution and σ_V is variance of the speed distribution.

The superposition of CCFs with different speeds and the same diffusion time is obtained by the weighted integration of Eq. (5).

$$\langle G\rangle_{X12}(\tau;\tau_D,\tau_{V0})=\frac{1}{\sqrt{2\pi}\sigma_V}\int G_{\mathrm{Diff}}(\tau;\tau_D)\times\exp\left[-\frac{1}{\omega_0^2}\frac{|\mathbf{R}-v\tau|^2}{\left(1+\frac{\tau}{\tau_D}\right)}\right]\exp\left[-\frac{(v-V_0)^2}{2\sigma_V^2}\right]\mathrm{d}v. \tag{8}$$

This integration can be done analytically leading to the following functional form:

$$\langle G\rangle_{X12}(\tau;\tau_D,\tau_{V0})=\frac{G_{\mathrm{Diff}}(\tau;\tau_D)}{\sqrt{1+\frac{\sigma_V^2\tau^2}{\omega_0^2\left(1+\frac{\tau}{\tau_D}\right)}}}\exp\left[-\frac{(|\mathbf{R}|-V_0\tau)^2}{\omega_0^2\left(1+\frac{\tau}{\tau_D}\right)+2\sigma_V^2\tau^2}\right]. \tag{9}$$

The presence of a distribution of drift speeds leads to inhomogenous widening of the CCF peak [see Fig. 1(a)]. From Eq. (9), we recover Eq. (5) in the limit $\sigma_V\to0$. We have simulated CCF curves (simulation parameters: $V_0=1000$ μm/s, $\tau_D=4$ ms, $|\mathbf{R}|=2$ μm, and $\omega_0=0.6$ μm) at increasing values of the ratio σ_V/V_0 and forced a fit of the curves to Eq. (5). In this way, we find effective values of the diffusion and drift times. The inhomogenous widening of the cross-correlation peak is rapidly increasing, as shown in Fig. 1(a). Simultaneously, we can observe a shift of the position of the maximum lag time, $\tau_{\max}$, to shorter values, particularly for $\sigma_V/V_0\geq0.4$. The agreement between the best fit average drift speed and V_0 is rapidly degrading when we increase the width of the speed distribution [20% underestimation for $\sigma_V/V_0\approx0.1$; open squares, Fig. 1(b)], whereas the diffusion time is still recovered quite well [filled circles, Fig. 1(b)]. In summary, in the presence of a smooth distribution of speeds, the average flow speed is underestimated when analyzing the CCFs according to Eq. (5). The diffusion time is instead well recovered.

When we follow sparse, large objects (much larger than the beam waist), the heterogeneity on the CCF decay becomes relevant. The relation between the width of the CCF peak and the diffusion coefficient of the objects is not ensured any more

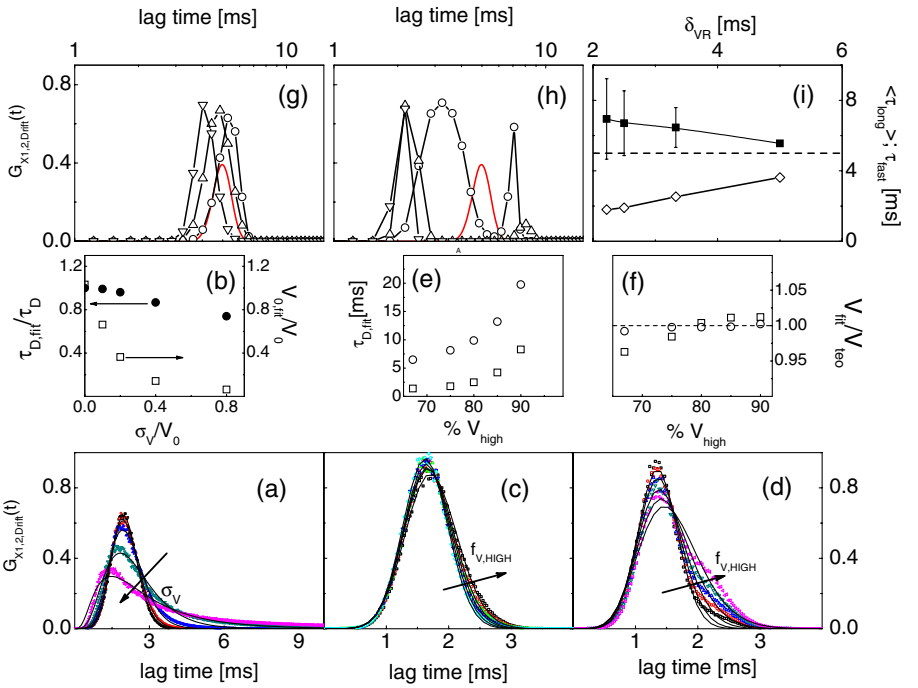

Fig. 1 Simulated cross-correlation $[G_{X1,2}(\tau)]$ functions (CCFs) for complex flows. Gaussian distributed noise (3%) was added to all the simulated CCFs. (a) and (b) refer to a Gaussian distribution of the modulus of the drift speed $|\mathbf{V}|$ [see Eqs. (8) and (9)]. (a) CCFs for increasing values of the distribution variance ($\sigma_V = 0$, 100, 200, 400, and 800 μm/s as indicated by the arrow; $V_0 = 1000$ μm/s, $\tau_D = 4$ ms). The solid lines are the best fit to Eq. (5). The best fit parameters, diffusion time ($\tau_{D,\text{fit}}$, filled circles), and drift speed ($V_{0,\text{fit}}$, open squares) are reported in (b) as a function of speed dispersion, σ_V/V_0. (c) and (d) report the CCFs simulated by superposing two flow components, $V_{\text{HIGH}} = 1250$ μm/s and $V_{\text{LOW}} = 1000$ μm/s (c) and $V_{\text{HIGH}} = 1500$ μm/s and $V_{\text{LOW}} = 1000$ μm/s (d), as a function of the weight of the high-speed component ($f_{\text{HIGH}} = 67$, 75, 80, 85, and 90%, as indicated by the arrow). The simulated CCF was computed as $G_{\text{simul}}(\tau) = f_{\text{HIGH}} G_{X12}(\tau; \infty, \tau_{V_{\text{HIGH}},R}) + (1 - f_{\text{HIGH}}) G_{X12}(\tau; \infty, \tau_{V_{\text{LOW}},R})$. No Brownian diffusion component was added ($\tau_D \cong 400$ s). The solid lines are best fit of Eq. (5) to the simulated data. The best fit parameters, diffusion time ($\tau_{D,\text{fit}}$), and drift speed ($V_{0,\text{fit}}$) are reported in (e) and (f), respectively (squares, $V_{\text{HIGH}} = 1500$ μm/s and circles, $V_{\text{HIGH}} = 1250$ μm/s). (g), (h), and (i) report the simulations of periodic flow CCFs [Eq. (10), $\tau_{VR} = 5$ ms; $\tau_D = 5$ ms, $|\mathbf{R}| = 10$ μm, $\omega_0 = 0.8$ μm, $\lambda = 0.8$ μm, $\phi = 0$, $\langle V \rangle = 2000$ μm/s]: $\delta_{VR} = 10$ ms [$\delta_V = 1000$ μm/s, panel (g)] and $\delta_{VR} = 3.3$ ms [$\delta_V = 3000$ μm/s, panel (h)]. Symbols refer to (circle, $\omega = 500$ Hz; up triangle, $\omega = 700$ Hz; down triangle, $\omega = 900$ Hz). The solid [red] continuous line refers to Eq. (5). (i) reports the maximum lag times for the two major components of the CCFs as a function of δ_{VR}. The dashed horizontal line indicates the drift time τ_{VR}; the solid lines are guides for the eye.

due to the limited statistics. Approximately 60 blood red cells are detected per second in the zebrafish embryos, compared to >700 per second for a highly diluted solution (1 nM) of fluorophores in a flow at speeds as high as $V = 1000$ μm/s. In this case, the diffusion time becomes an effective parameter that effectively measures the fluctuations in the object trajectory arising, for example, from its interaction with the vessel wall rather than its translational diffusion. This may occur, for example, when studying blood flow by monitoring red blood cells in vessels.

We have simulated this condition by superimposing only two closely spaced drift speed components with speeds V_{HIGH} and V_{LOW} and by varying their relative weights [see Figs. 1(c) and 1(d)]. We have assumed different speed values simply in order to simulate different drift times, τ_{VR}, arising from fluctuation in the objects trajectories. We have then added 3% of Gaussian noise to the resulting CCFs in order to simulate realistic data sets. Since we want to simulate micron-sized objects with very low diffusion coefficients, we have abolished the contribution of the diffusion dynamics by assuming $\tau_D = 400$ s in the simulations. Any broadening of the CCF drift peak is then due to the heterogeneity of the drift time. We have accordingly force fitted the simulated CCFs to Eq. (5) leaving both the diffusion time and the drift speed as free fit parameters.

The best fit parameters of the forced fit are reported in Fig. 1(e) (diffusion time) and Fig. 1(f) (drift speed) as a function of the relative weight of the higher speed component (f_{HIGH} is the fraction assigned to the high speed in the simulated CCF). We have explored two speed ratios: $V_{\text{HIGH}}/V_{\text{LOW}} = 1.25$ [Fig. 1(c)] and 1.5 [Fig. 1(d)]. In both cases, the best fit diffusion time obtained by fitting the simulated cross-correlation to Eq. (5) appears to be an effective parameter that measures the widening of the cross-correlation peak arising from the presence of two closely spaced components. It is noteworthy that this effective diffusion time, $\tau_{D,\text{fit}}$, increases with the relative weight of the higher-speed component. Notably the larger effective diffusion time is found for the smaller ratio $V_{\text{HIGH}}/V_{\text{LOW}} = 1.25$ [open circles in Fig. 1(e)] and it can be as high as 19 ms. The drift speed is instead very close to the weighted value, $V_{\text{teo}} = f_{\text{HIGH}} V_{\text{HIGH}} + (1 - f_{\text{HIGH}}) V_{\text{LOW}}$ [see Fig. 1(f)].

The relevant result of these simulations is that for diluted suspensions of large colloids (such as red blood cells in small capillaries), the diffusion time is an effective parameter not directly related to the translational diffusion, whereas the average drift speed is well recovered in all cases explored here.

A third case occurs when the drift speed changes periodically in time. In the case of blood, the pulsation is composed of systolic (ventricular contraction) and diastolic (atrial contraction) phases that cover $\sim 1/3$ and $2/3$ of the pulsation period, respectively.[22,24–26] For zebrafish embryos between two and four days postfertilization (d.p.f.), the pulsation period is ~300 to 500 ms.[26] Therefore, both diastole and systole last much longer than typical drift times ≈10 to 40 ms, observed in zebrafish embryos. In this case, the speed flow does not change substantially during the flight of red blood cells between the two observation volumes and we can approximate the CCF as the sum of two drift components with speeds equal to the diastole and systole flow speeds, as done in the literature.[22,25]

However, it is of some interest, particularly for *in vitro* applications, to assess the effect of the periodicity of the flow on the computed CCFs when the average time of flight is not much shorter than the pulsation period. We have computed analytically the CCF decay for a harmonic variation of the flow. We assume a flow speed varying in time as $V(t) = \langle V \rangle + \delta_V \cos(\omega t + \phi) = |\mathbf{R}|[(1/\tau_{VR}) + (1/\delta_{VR})\cos(\omega t + \phi)]$. $\langle V \rangle$ and δ_V are the average value and modulation of the flow speed. The angular frequency and the phase shift of the speed modulation are ω and ϕ. δ_{VR} is the modulation of the drift time in flow speed modulation simulations. The times δ_{VR} and τ_{VR} are related to these values by the relations $\delta_V = |\mathbf{R}|/\delta_{VR}$ and $\langle V \rangle = |\mathbf{R}|/\tau_{VR}$. Within this assumption, we compute the following CCF functional form:

$$G_{X12}(\tau;\tau_D,\tau_{VR}) = G_{\mathrm{Diff}}(\tau;\tau_D) \times \exp\left\{-\frac{|\mathbf{R}|^2}{\omega_0^2}\frac{\left|1-\frac{\tau}{\tau_{VR}}-\frac{[\sin(\omega\tau)\cos(\phi)-2\,\sin(\phi)\sin^2(\omega\tau/2)]}{\omega\delta_{VR}}\right|^2}{\left(1+\frac{\tau}{\tau_D}\right)}\right\}. \quad (10)$$

For small values of speed modulation $|\mathbf{R}|/\delta_{VR} \approx 1000$ μm/s and high frequency ($\omega/\tau_{VR} \approx 0.5$ to 4.5) we observe a single peak [Fig. 1(g)] in CCFs simulated according to Eq. (10). The width of the CCF peak does not change substantially and the maximum position is shifted from above τ_{VR} (for $\omega \approx 500$ Hz) to below τ_{VR} [for $\omega \approx 700$ Hz, Fig. 1(g)]. At increasing amplitude of the speed modulation $|\mathbf{R}|/\delta_{VR} \approx 3000$ μm/s [Fig. 1(h)], up to three components are observed in the CCF. One or two components invariably fall at lag times shorter than τ_{VR}, corresponding to the maximum speed reached by the flow, and occur within ≈30% from each other in all the cases explored here [Fig. 1(h)]. The third component of the CCF lies always at lag times longer than τ_{VR}. The average lag time of the two faster components and the lag time of the slower component approach, from above and from below, respectively, the average value τ_{VR} for $\delta_V = |\mathbf{R}|/\delta_{VR}$ approaching zero [see Fig. 1(i)]. The main result of these simulations is that under harmonic pulsatile flow, the CCFs do show multiple drift components that may not accurately reproduce the maximum and minimum flow speeds.

3 Materials and Methods

3.1 *Optical Setup*

The dual-beam FCS experiments have been performed on a home-made setup in which a Ti:Sa mode-locked laser source (Tsunami, Spectra Physics, Santa Clara, California) primes two photon excitation on the sample. A wide-field image of the focal plane is collected by an EM-CCD (Cascade II – 512B, Princeton). The scanning of the sample is ensured by a home-made purely reflective scanning head optimized for the 0.75 to 1.5 μm laser band width. Two galvo mirrors (6350, Cambridge Technology, Watertown, Massachusetts) have been coupled to the entrance pupil of the microscope objective by means of two 3-in. spherical mirrors with focal lengths of 75 and 150 mm. These mirrors correct for the astigmatism arising from the finite distance between the two galvo mirrors, while a long focal length lens (achromatic doublet, $f = 400$ mm) right below the microscope objective corrects for the beam ellipticity. A 20× objective (NA = 0.95, working distance = 2 mm, 20×, water immersion, XLUMPlan FI, Olympus, Tokyo, Japan), optimized for the near-infrared region, was used for the cross-correlation measurements.

The laser beam is split in two independently steerable beams by a Twyman-Green interferometer. The plane of the two mirrors of the interferometer is conjugated to the objective back aperture by two lenses acting as a telescope. This setup allows us to position the two focal volumes in the sample by tilting the mirrors of the interferometer. The microscope objective is used in epifluorescence illumination: fluorescence emission is gathered from the same objective and an image is formed on the EM-CCD detector. The EM-CCD has a 512×512 pixel sensible chip and is designed to acquire in frame transfer mode, reaching a frame rate of 250 fps for subregions with <20 pixel linear size. Such a frame rate determines a maximum time resolution, for the cross-correlation measure, of 4 ms.

For cross-correlation test measurements, a borosilicate capillary tube (CM Scientific Ltd., Silsden, United Kingdom) with square section is used, with an inner section of 800×800 μm (160 μm wall thickness). The square section was chosen to minimize aberrations in the focal volume. The laminar flow of the solutions in the capillary is obtained by connecting both sides of the capillary tube to 4 cm^3 glass cylinders used as the sample reservoirs. These cylinders are set horizontally and at different heights by a micrometric regulation. The flow speed from the upper cylinder to the lower one through the capillary tube can be changed by varying the relative height of the two reservoirs. Surface tension prevents the sample solution from spilling from the cylinders.

3.2 *Chemicals and Embryos*

Rhodamine 6G and Fluorobrite microspheres, 30 nm in size, were acquired from Sigma-Aldrich and used without further purification. Rhodamine 6G stock solutions in ethanol were diluted to 20 to 40 nM concentration for correlation measurements. Gold nanorods were synthesized by means of the seed growth method in the presence of cetyl trimethylammonium bromide surfactant as described elsewhere.[27]

All the cross-correlation measurements on zebrafish embryos (one to four d.p.f.) were performed on embryos of the transgenic line $mitfa^{w2/w2}$; $roy^{a9/a9}$; $Tg(kdrl{:}\mathrm{EGFP})^{s843}$; $Tg(\mathrm{gata1{:}dsRed})^{sd2}$, carrying green-labeled epithelium (EGFP)

and red-labeled (dsRed) red blood cells. A mutant transgenic line expressing only EGFP in the endothelial cells, mitfa$^{w2/w2}$; roy$^{a9/a9}$; $Tg(kdrl{:}\mathrm{EGFP})^{s843}$, was used to obtain confocal images for validation purposes.[28] The zebrafish embryos were anesthetized with tricaine [40 mg/l tricaine (Ethyl 3-aminobenzene methansulfonate, Sigma-Aldrich Corporation, St. Louis, Missouri)][29] and positioned in a 2-mm-diam fluorinated ethylene propylene tube (FT2X3, Adtech Polymer Engineering, Frampton Mansell, United Kingdom) with 1.5% low melting point agarose and then immersed in a water cell.[30]

4 Results

4.1 *In Vitro Experiments*

By means of EM-CCD based detection we can measure drift speeds of tracers in a wide range of speeds since the setup allows us to easily change the distance between the observation volumes. We first analyzed two suspensions flowing in borosilicate capillaries ($800 \times 800\ \mu m^2$ in section). Rhodamine 6G in water was taken as a high diffusion coefficient reference sample ($D_{20C} \cong 340 \times 10^{-12}\ m^2/s$)[15] and 16 nm × 48 nm gold nanorods in water were taken as a low diffusion coefficient reference sample [$D \cong (12 \pm 2) \times 10^{-12} m^2/s$, hydrodynamic radius 18 ± 3nm, axial ratio ≅ 3.3).[27] Fluorescence emission in both samples was primed by two-photon absorption at $\lambda_{exc} = 0.8\ \mu m$.[31]

4.1.1 *Cross-correlation as a function of the interspot distance*

We used the gold nanorod suspensions as a test of the invariance of the flow speed measurement on the distance between the two spots. The actual value of the speed, $V_{exp} = 280 \pm 50\ \mu m/s$, was obtained by directly measuring the volumetric rate of the hydraulic system. Cross-correlation functions were computed at different distances between the excitation spots in the range of $3\ \mu m \le |\mathbf{R}| \le 17\ \mu m$ [Fig. 2(a)]. The functions can be well described by Eq. (5) [see Fig. 2(a), solid lines], and the separate fits of the four CCFs give best fit drift times τ_{VR} that depend linearly on the interspot distance up to $|\mathbf{R}| \cong 20\ \mu m$ [see Fig. 2(b)]. The slope of the linear trend corresponds to an average drift speed $V_{fit} = 280 \pm 10\ \mu m/s$ and diffusion time obtained from the best fit of the CCFs is $\tau_{D,fit} = 3 \pm 0.5$ ms (the uncertainty corresponds to the standard deviation computed over different interspot distances). A global fit to the whole set of CCFs leads to very similar results (best fit $\tau_{D,fit} = 3$ ms, $V_{fit} = 270 \pm 80\ \mu m/s$). The drift speed is very well retrieved from the analysis of the CCFs in a wide range of the τ_{VR}/τ_D ratio [$2.5 \le \tau_{VR}/\tau_D \le 17$; upper inset of Fig. 2(b)]. The best fit slope in the inset of Fig. 2(b) is $\partial(\tau_{VR}/\tau_D)/\partial|\mathbf{R}| = (1.3 \pm 0.1)\ \mu m^{-1}$, in good agreement with the expected value of the ratio $8D/V\omega_0^2 = 1.0 \pm 0.2\ \mu m^{-1}$ [$\omega_0 = 0.6\ \mu m$, $V = 270\ \mu m/s$, $D = (12 \pm 2) \times 10^{-12}\ m^2/s$]. It is noteworthy that, according to the numerical simulations reported above, the range of drift times investigated corresponds to $\Gamma = \tau_{VD}/\tau_D = 0.4$ to 0.75, leading to a maximum 5% correction to τ_{max} with respect to τ_{VR} [see Eq. (6)].

Limitations on the maximum interspot distance are set by the microscope objective F number and magnification. For the 20× objective used here, the maximum interspot distance is $|\mathbf{R}| \approx 50\ \mu m$. Very small interspot distances ($|\mathbf{R}| < 2\omega_0$) cause leakage of signals between the two spots leading to autocorrelation components in the cross-correlation functions and

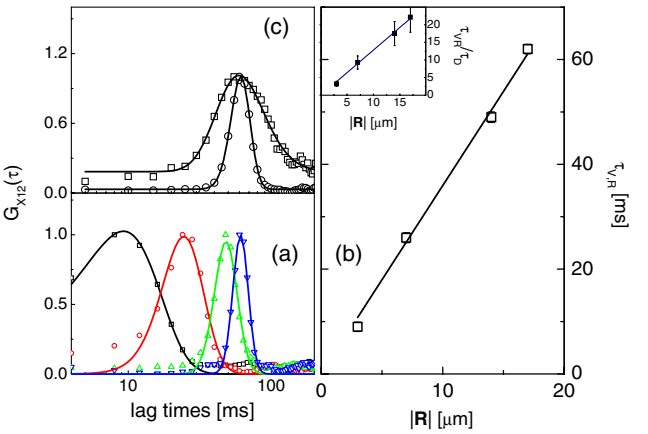

Fig. 2 Experiments on gold nanorods (≈16 nm × 48 nm) in square microcapillary. (a) Normalized CCFs acquired from spots at distances $|\mathbf{R}| = 3, 4, 14, 17\ \mu m$ (squares, circles, up and down triangles, respectively), collinear to the flow in the microcapillary. Solid lines are best fit of Eq. (5) to data ($\omega_0 = 0.6\ \mu m$; $\lambda_{exc} = 0.8\ \mu m$). (b) reports the best fit values of the flow speed obtained from τ_{VR} as a function of $|\mathbf{R}|$. The solid line is the best fit with slope 3.59 ± 0.04 ms/μm. Inset: ratio of the best fit drift over diffusion times τ_{VR}/τ_D as a function of the interspot distance. The solid line is the linear trend $\tau_{VR}/\tau_D = |\mathbf{R}|(8D/V\omega_0^2) \approx |\mathbf{R}|(1.3 \pm 0.1)$. (c) Normalized cross-correlation signal from gold nanorods (circles, $|\mathbf{R}| = 12\ \mu m$), and rhodamine 6G (squares, $|\mathbf{R}| = 24\ \mu m$) in water solution (beam waist $\omega_0 = 0.6\ \mu m$). Solid lines are the best fit to Eq. (5). Fitted diffusion coefficients are $(310 \pm 30) \times 10^{-12}\ m^2/s$ for rhodamine 6G and $(13 \pm 1) \times 10^{-12}\ m^2/s$ for gold nanorods. The best fit drift speeds are $V = 310 \pm 10\ \mu m/s$ and $V = 195 \pm 2\ \mu m/s$ for the rhodamine 6G and the nanorods suspension, respectively.

a larger uncertainty on the best fit drift parameters. These spatial limitations ($|\mathbf{R}| \ge 4\omega_0$) couple to the time requirement given by the CCD (minimum image sampling time $\tau_s = 4$ ms). In fact, the CCF trend at small lag times is approximately Gaussian, $G(m) \propto S\ \exp[-(|\mathbf{R}|^2/\omega_0^2)|1 - (m\tau_S/\tau_{VR})|^2]$, and its amplitude ($S$) is typically 10 times the noise ($S \approx 10N$). For the sake of simplicity, we measure the drift time in terms of the sampling time, τ_S, as $\tau_{VR} = M\ \tau_S$. If we now require that the CCF peak is well above the noise level for at least three lag time points, the maximum and two adjacent ones [i.e., $G(M \pm 1) > N$), we come to an analytical estimate of the minimum measurable drift time that we write as $M \ge (R/\omega_0)/\sqrt{\ln(S/N)}$. Therefore, for $S/N = 10$, $(R/\omega_0) = 4$, and $\tau_S = 4$ ms, we cannot reliably measure drift times, τ_{VR}, <10 ms. These limitations lead to maximum measurable values of flow speed of about $V_{max} \cong 6000\ \mu m/s$ for our setup.

4.1.2 *Cross-correlation as a function of the diffusion coefficient*

Cross-correlation analysis can provide information on the diffusion coefficient of the fluorophore beyond the time resolution of the detector by exploiting the weak dependence of the cross-correlation peak width on the diffusion coefficient.[15] For this purpose, we compared CCFs measured on rhodamine 6G solutions to those measured on suspensions of gold nanorods [see Fig. 2(c)]. In Fig. 2(c), we report two CCFs acquired with slightly different parameters ($|\mathbf{V}|$ and $|\mathbf{R}|$) in order to visually obtain a good superposition of the cross-correlation peak. The data fit to Eq. (5) provides best fit drift speeds of $V = 310 \pm 10\ \mu m/s$ and $V = 195 \pm 2\ \mu m/s$ for the rhodamine

6G and the nanorods suspension, respectively. The best fit diffusion coefficients ($T = 22$°C) are $(310 \pm 30) \times 10^{-12}$ m^2/s for rhodamine 6G and $(12 \pm 1) \times 10^{-12}$ m^2/s for gold nanorods. Both results are compatible with literature and our independent estimates.[15,27,32] It must be noted that rhodamine 6G diffusion time on a 0.6-μm beam waist is $\cong$75 μs, which is much smaller than our sampling time. Finally, we notice that, according to Eq. (6), the peak lag time of the cross-correlation underestimates the drift time τ_{VR} only by 0.1% for gold nanorods. For rhodamine 6G, instead, the drift time underestimation rises to 6%.

4.1.3 *Cross-correlation as a function of the drift speed*

We computed fluorescence CCF for fluorescent microbeads dispersed in water and flowing in a borosilicate square section capillary. The drift speed was changed by microregulating the height, H, between two vessels (insulin syringes) connected with a 800 μm inner diameter Teflon tube to the capillary. We have varied the relative height of the two vessels from $H = -3500$ μm to $H = +5000$ μm (sketch in Fig. 3). The analysis of the CCFs acquired as a function of H reveals three regimes. At negative values of H, ($-3500\,\mu\text{m} \le H \le -1000\,\mu\text{m}$), we find a linear dependence of the drift speed on H, with slope $-(0.55 \pm 0.08)$ s^{-1}, as we should expect in a Poiseuille flow regime.[6] At intermediate values of the relative height we could not measure any cross-correlation between the spots. In this case, wall adhesion and capillary effects[33–35] interfere severely with the viscous flow and the fluid speed effectively vanishes. The estimate of the capillary pressure to be overcome, due to adhesion between water and the wall of the syringe, is $\approx 4(\gamma_{sg} - \gamma_{sl})/d_S$, where γ_{sg} and γ_{sl} are the surface tensions between plastic (solid) and air (gas), and between plastic and water (liquid) and d_S is the reservoir diameter ($d_S \approx 4000$ μm). For poly(methyl methacrylate) (PMMA),[35] $(\gamma_{sg} - \gamma_{sl}) \approx 0.02$ J/m^2 and the pressure difference amounts to ~ -20 N/m^2. This value corresponds to 2000 μm of water height that compares well with the height gap in which we cannot measure any water flow ($\approx$3000 μm).

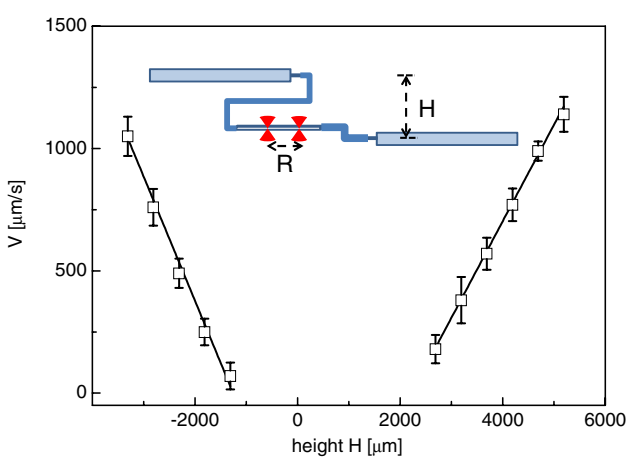

Fig. 3 Drift velocity measured on 30 nm fluorescent nanosphere suspensions flowing through a square capillary (size = 720 ± 20 μm) as a function of the difference in height (H) between the two reservoirs. The distance between the two laser spots (hourglass symbols in the sketch) is $|\mathbf{R}| = 16$ μm. The CCFs were fit to Eq. (5). The solid lines correspond to the linear fit to the drift speeds in the two regions $H > 0$ (slope = 0.42 ± 0.12) s^{-1} and $H < 0$ (slope = -0.55 ± 0.08 s^{-1}).

In the third region, at (2500 $\mu\text{m} \le H \le 5000$ μm), we can measure a clear cross-correlation peak in the reverse CCF $G_{X21}(\tau)$ and the fluid speed again scales linearly with height difference, with a slope of (0.42 ± 0.12) s^{-1}. These values can be compared to the prediction made according to Poiseuille law for a square capillary of size d,[35] connected to two reservoirs. The flow is determined by the pressure gradient due to the relative height, H, of the two reservoirs, $\Delta P = \rho g H/L$, where ρ is the density of the fluid, here taken as that of water, g is the gravity acceleration, and the tubing length is $L \approx 0.69$ m in our setup. The estimated maximum speed in the capillary is then $V_{\max}(H) = H[(\rho g/L\eta)0.084]d^2$. For the present case (the real size of the capillary is $(d = 720 \pm 40$ μm), the prediction $V_{\max}(H)/H = (0.60 \pm 0.06)$ s^{-1} is in reasonable agreement with our experimental findings $V_{\max}(H)/H = (0.51 \pm 0.07)$ s^{-1}.

4.1.4 *Speed profile across the capillary section*

The benefits of the EM-CCD dual-beam cross-correlation setup for parallel acquisition can be better estimated when extended excitation patterns are employed. To provide an example of this application, we have combined line scanning with our dual-beam setup. For this purpose, the line scanning rate is implemented at 200 lines/s and synchronized with the image acquisition rate. In this way, we have the possibility to perform, on a single image, cross-correlation along the flow direction over a range of radial positions in the capillary section that is limited only by the field of view. The only spatial limitation in this case is posed by the size of the pixel on the CCD chip that corresponds to 7.4 μm on the sample. Since the line scanning is performed synchronously with the image acquisition, our configuration is equivalent to shining an irradiation pattern composed of two parallel laser lines perpendicular to the capillary axis. We describe the two scanned lines as a set of pixels, $\{\{P_1[i_1]\}_{i_1=1\ldots N}\{P_2[i_2]\}_{i_2=1\ldots N}\}$, where the subscripts indicate the line and the index i_1 or i_2 the order of the pixel along each line, composed of N total pixels. The CCFs were computed between two pixels of the two lines along the flow, $G_{X1,2}^{(i1.i2)}(\tau) = \langle I_{1,i1}(\tau) I_{2,i2}(0)\rangle - \langle I_{1,i1}(0)\rangle\langle I_{2,i2}(0)\rangle$. With a 20× microscope objective we have sampled almost half of the section of the square capillary (Fig. 4) over $N = 42$ pixels.

We measured the flow speed directly from the lag time of the maximum of the CCFs $G_{X1,2}^{(i1=i2)}(\tau)$. The flow speed values as a function of the radial distance (z) from the center of the capillary (Fig. 4) have then been fit to the following trial function (see Fig. 4, sketch):[35]

$$V(z) = V_{\max} \sin\left[\pi \frac{(z - z_0)}{d}\right]. \tag{10}$$

In this equation, which is an extension of the known parabolic profile observed in circular cross-section capillaries, d and $V_{\max}$ are the size of the capillary and the maximum speed of the fluid (at the center of the capillary). The position of the center of the capillary section is not known and is used as a best fit parameter z_0, which is the radial coordinate of the maximum speed in the capillary. The best fit of Eq. (10) to the data reported in Fig. 4 (continuous line) gives $d = 720 \pm 20$ μm, $V_{\max} = 464 \pm 5$ μm/s, and $z_0 = 48 \pm 2$ μm.

This fit offers an estimate of the actual internal size of the microcapillary that is 10% lower than nominal data. The forced fit of the data in Fig. 4 to Eq. (10) while keeping d fixed at

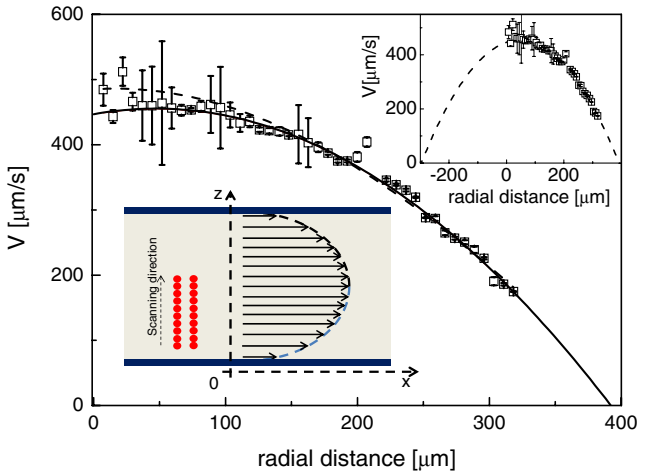

Fig. 4 Characterization of the speed profile of the section of the glass square capillary. The flow speed was obtained directly from the lag time of the maximum of the CCFs $G_{X1,2}^{(i1=i2)}(\tau)$. The CCFs over almost half of the capillary section were computed in parallel on two corresponding spots lying along the flow direction that were scanned in a direction perpendicular to that (see sketch). The solid line is the best fit to the data of Eq. (10) with best fit values of $z0 = 48 \pm 2$ μm, $d = 720 \pm 20$ μm, and $V_{max} = 464 \pm 5$ μm/s. The dashed line is the best fit of the data to Eq. (10) with d kept fixed at 800 μm. The inset reports the data superimposed on the extrapolation of the best fit profile over the whole capillary width.

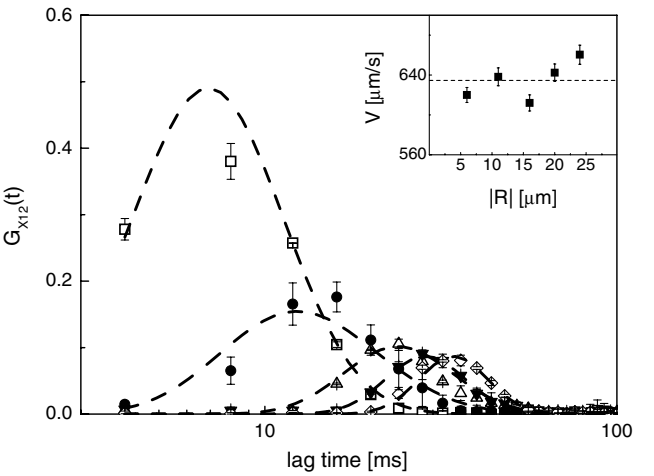

Fig. 5 CCFs computed on vein blood vessels of a zebrafish embryo (four days postfertilization) at increasing values of the distances between the laser spots. The different symbols refer to $|\mathbf{R}| = 6$ μm (open square), 11 μm (filled circles), 16 μm (open up-triangles), 20 μm (filled down-triangles), and 24 μm (open diamonds). The error bars correspond to an average over three different measurements on the same embryo. The dashed lines are the best fit curve to Eq. (5). The inset reports the best fit values of the drift speed obtained from fitting the cross-correlation to Eq. (5). The dashed line indicates the speed average value.

the nominal size $d = 800$ μm gives clearly unsatisfactory results (Fig. 4 dashed line).

We finally notice that we could have fit each $G_{X1,2}^{(i1=i2)}(\tau)$ function to Eq. (5) to measure drift times and flow speeds. However, this time-consuming procedure leads to drift times that are underestimated with respect to the maximum CCF lag time by only 0.3% (0.9%) at the maximum (minimum) of the flow speed profile.

4.2 *Experiments on Zebrafish Embryos*

4.2.1 *Blood flow can be followed by cross-correlations along the vein*

We applied CCD cross-correlation spectroscopy to study blood flow in zebrafish embryos vessels. For this purpose, we have employed transgenic embryos whose blood red cells carry dsRed protein. dsRed fluorescence is primed by two-photon excitation at $\lambda_{exc} = 0.9$ μm and the emission is collected at $\lambda_{em} = 0.6$ μm through a HQ600/40 filter (Chroma, Bellows Falls, Vermont). The two spots of the infrared laser were set at variable distances along the vessel axis in the middle of the vessel cross-section and along the blood flow direction. Coarse adjustment of the spots along the flow lines was reached by moving the embryo and finer tuning was obtained by moving one of the spots in the focal plane by means of the interferometer mirrors.

We tested at first the accuracy of the blood flow speed measurements on a single embryo by performing repeated measurements on the embryo's vein at increasing distances between spots. All the CCFs have been analyzed according to Eq. (5) in the range of 6 μm $\leq |\mathbf{R}| \leq$ 24 μm (Fig. 5), and in this range, the average value is determined with <3% uncertainty on the single embryo. The data reported in Fig. 5 correspond to a 4 d.p.f. embryo and $|\mathbf{V}| = 640 \pm 20$ μm/s (3% uncertainty). The diffusion time in the analysis of all the CCFs is kept at $\tau_D \approx 0.1$ ms. As discussed previously in the text, this parameter has to be taken, for sparse samples with rare fluorescence bursts, as an effective value that describes the random superposition of a few, distinct, cross-correlation peaks [Figs. 1(c), 1(d), and 1(e)].

4.2.2 *Discrimination of systolic and diastolic phases*

We move to the study qualitative and quantitative differences in the blood flow along the caudal vein and the dorsal aorta. For this purpose, we should evaluate the biological variability of the data. We have taken averages of the flow parameters over three to four different embryos at the same developmental stage.

From the fluido-dynamics point of view, the major difference between the two vessels is the presence of a double peak in the CCF measured on the artery. In the vein, far from the tail, we find a single peak that corresponds to a drift speed of $V_{vein} = 630 \pm 70$ μm/s [Fig. 6(a)]. On the contrary, in the artery, two peaks in the CCFs are found [Figs. 6(b) and 6(c)], suggesting the presence of two phases in the blood flow. According to the literature,[22,25] these phases can be ascribed to the systole (faster phase) and diastole (slower phase) phases. We have then analyzed the data taken in the embryo artery according to a drift model [Eq. (5)] with two drift components (the same diffusion time was taken for both the drift components of the CCFs) at different distances from the tail capillary bed.

The CCFs collected at half way (50% distance, see image in Fig. 6) of the heart-tail distance are reported in Fig. 6(c). The analysis of these functions gives $V_{syst} = 1420 \pm 200$ μm/s and $V_{diast} = 380 \pm 20$ μm/s. When we perform the same experiment at 20% of the tail-heart distance, we still obtain two drift components with much more closely spaced speed values [see Fig. 6(b)]. The average values of the systole and diastole speeds are, in this case, $V_{syst} = 980 \pm 120$ μm/s and $V_{diast} = 420 \pm 40$ μm/s. The systolic component shows a larger decrease when approaching the tail, compared to the diastolic component that is almost constant. The averages taken over

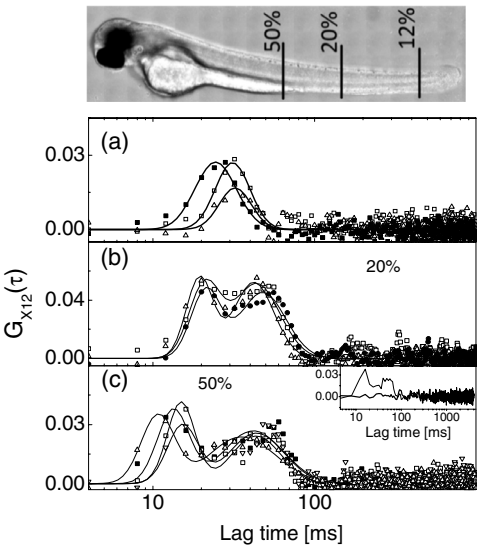

Fig. 6 CCFs measured in vessels of different zebrafish embryos at four days postfertilization (d.p.f.) ($|\mathbf{R}| = 20\ \mu$m). Examples of CCFs measured in the vein are reported in (a) together with their best fits [Eq. (5), solid lines]. The average value of the drift speed $V_{vein} = 630 \pm 70\ \mu$m/s. Examples of the CCFs measured in the artery close (20% tail-heart distance, see image) to embryo's tail are reported in (b). The average value of the best fit systolic and diastolic speeds are $V_{syst} = 980 \pm 120\ \mu$m/s and $V_{diast} = 420 \pm 40\ \mu$m/s, respectively. Examples of the CCFs computed in the artery at half way between embryo heart (50% tail-heart distance, see image) are reported in panel (c). The average value of the best fit systolic and diastolic speeds are $V_{syst} = 1420 \pm 200\ \mu$m/s and $V_{diast} = 380 \pm 20\ \mu$m/s, respectively. Inset in panel (c) report the comparison of the CCFs $G_{X12}(t)$ (thin line) and $G_{X21}(t)$ (thick line). The latter function does not show a correlation peak, confirming the direction of the flow. The image reports the transmitted light image of a zebrafish embryo at 4 d.p.f. (size $\approx$ 3.5 mm).

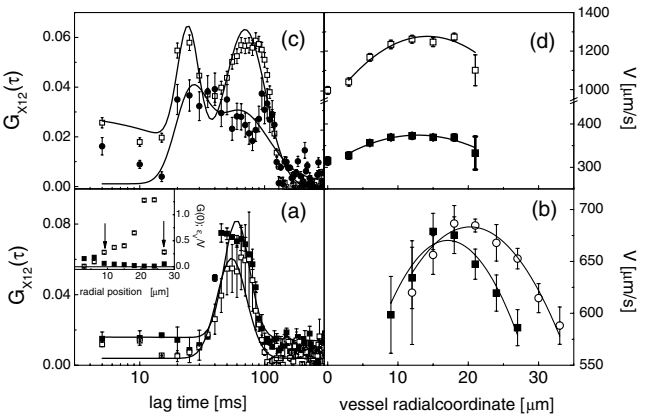

Fig. 7 Speed profile across veins and arteries measured at 50% of heart-tail distance in zebrafish embryos (developmental stage: 4 d.p.f., $|\mathbf{R}| = 40\ \mu$m). (a) reports two exemplary CCFs measured in zebrafish veins at a distance $\approx 0.25 d_V$ (open squares) and $\approx 0.125 d_V$ (filled squares) from the vessel wall (d_V is the estimated vessel diameter). Solid lines are the best fit to Eq. (5) with a single drift component. Inset: plot of the CCF amplitude, G(0), and the drift speed uncertainty, ε_V/V, obtained from the data fitting as a function of the radial distance across the vessel. The vertical arrows indicate the estimated position of the vessel wall. (b) Profile of the best fit speed values in veins measured on two (4 d.p.f.) zebrafish embryos. Each set of data is the average of three different scanning on the same embryo. The solid line is the best fit of the data to the trial function $V(r) = V(r_0) - [V(r_0) - V(r_0 \pm d_V/2)][2(r - r_0)/d_V]^2$ (see text). (c) Two exemplary CCFs measured in zebrafish arteries at $\approx 0.25 d_V$ (open squares) and $\approx 0.125 d_V$ (filled squares) from the vessel wall. Solid lines are best fit to Eq. (5) with two drift components corresponding to the systole (higher values) and diastole (lower values). (d) Profile of the best fit speed values (open squares, systole and filled squares, diastole) measured on a 4 d.p.f. zebrafish embryo. The data are the average of three different scanning on the same embryo. The solid line is a parabolic fit to the data according to the same trial function as in (b).

three to four different embryos at the same developmental stage show larger uncertainty (10%) than those obtained from repeated blood flow speed measurements on the same embryo. The figure of 10 to 12%, therefore, represents the biological uncertainty on the blood flow measurements.

4.2.3 *EM-CCD cross-correlation estimate strain rate in the microvessels*

Plasma shear stress is a relevant parameter for hemodynamics since it can trigger the response of a number of proteins on the vessel epithelium.[22,36,37] In the literature, various methods have been applied to monitor the flow speed in microfluidic setups and even in animal models.[38–41] Beside a few applications of laser speckle imaging,[42] fluorescence detection in cytometry[43] and nuclear magnetic resonance (NMR),[44] PIV[26,37,39–41] has been widely applied to follow injected nanospheres and platelets and/or blood red cells observed in transmission optical microscopy and tomography.[45] Microinjection of particles needed for PIV could alter physiology due to unavoidable spheres' aggregation,[38] and correlation methods applied to cells flowing in the blood stream should be preferred for physiologically relevant insights.[45]

We measured CCFs of red blood cells fluorescence both in the dorsal vein and in the caudal aorta at half way between the zebrafish tail and heart, far enough from the pulsation origin (the heart) and the tail capillary bed, which has a large hydraulic compliance. The edges of the vessel were detected by following the abrupt fall of the value of the CCF amplitude $G(0)$, and the parallel increase in the relative uncertainty on the drift speed $[\varepsilon_V/V$ in the inset of Fig. 7(a), where ε_V is the standard deviation of blood flow speed as from the best fit of the CCFs], that occurs when we focus the laser spots outside the vessel (see Fig. 7(a), vertical arrows). For each pixel, the CCFs were fit to Eq. (5) with one [for the vein, Fig. 7(a)] or two [for the artery, Fig. 7(c)] drift components. We have checked that the blood flow was perpendicular to the two scanned lines across the vessel by computing CCFs of adjacent pixels, $G_{X1,2}^{(i\cdot i\pm 1)}(\tau)$ and $G_{X1,2}^{(i\cdot i\pm 1)}(\tau)$. The amplitude of the CCF decreased by increasing distances between the pixels with $G_{X1,2}^{(i\cdot i)}(0) = 0.08 \pm 0.01$, which is larger than $G_{X1,2}^{(i\cdot i-1)}(0) \cong G_{X1,2}^{(i\cdot i+1)}(0) = 0.042 \pm 0.005$ and $G_{X1,2}^{(i\cdot i+2)}(0) \cong G_{X1,2}^{(i\cdot i-2)}(0) = 0.009 \pm 0.004$.

The radial profile of the speed is well reproduced in embryos of similar ages [Fig. 7(b)]. We assume a linear relationship between the shear stress and the strain rate. In this way, we can obtain the shear stress[46,47] from the measurement of the steepness of the flow speed profile in the vessels of zebrafish embryos. We measure here an effective shear stress since we are following the motion of red blood cells (RBCs) that are comparable in size with the vessel diameter. The maximum effective strain rate in the vein, $\gamma = |(\partial V/\partial r)[r_0 \pm (d_V/2)]| = 4\{V(r_0) - V[r_0 \pm (d_V/2)]\}/d_V = 15 \pm 3\ \mathrm{s}^{-1}$, is

intermediate to those relative to the systole and diastole pulses measured in the artery, $|(\partial V/\partial r)[r_0 \pm (d_V/2)]| = 34 \pm 6\ \mathrm{s}^{-1}$ (systole) and $|(\partial V/\partial r)[r_0 \pm (d_V/2)]| = 8 \pm 3\ \mathrm{s}^{-1}$ (diastole). This can be due to the fact that the heart pulsation is much more effective in the artery than in the vein[26] and that the volumetric flow rate is much lower in the systole than in the diastole phase.[24] The values of the strain rate found here, when converted to shear stress (RBC viscosity $\approx 5 \times 10^{-3}$ Pa · s),[46] give values ≈0.05 to 0.15 Pa that are lower than those (≈1 Pa) derived for rabbit arterioles (larger than zebrafish vessels) by Tangelder et al.[37] and those measured in the aortic arch in zebrafish 4 d.p.f. by Chen et al. by μ-PIV.[26] These studies correspond, however, to higher pressures and reproduced the speed profile more closely than was done here since the tracked object (platelets or microbeads) is much smaller than the vessel diameter. Moreover, one should take into account that the wall shear stress measurement based on RBC tracking is an effective value.[47]

As shown in Figs. 7(b) and 7(d), the measured speed does not vanish at the edge of the vessel and the ratio of maximum velocity to the marginal velocity is $\chi = V(r_0)/V(r_0 \pm d_V/2) \approx 1.2 \pm 0.05$ for both the vessels. This has been observed earlier[37,47–49] in similar cases. Zhong and coworkers[48] reported detailed speed profiles in 32- to 120-μm-diameter retina veins obtained by tracing the motion of red blood cells on optical scanning microscopy images, finding $\chi \approx 1.36$ for 32 μm diameter capillaries and $\chi \approx 2$ for very large capillaries (the values should tend to infinity in a Poiseuille regime). A model developed by Yen et al.[50] and generalized by Zhong et al.[48] relates χ to the vessel diameter d_V.

$$\chi \cong 2(1 - 0.5328 \exp\lfloor -\sqrt{0.00435 d_V} \rfloor). \tag{11}$$

In our case, the vessel diameter is $d_V \approx 12 \pm 2$ μm for the vein and $d_V \approx 13 \pm 3$ μm for the aorta at midway between the tail and the heart, leading to $\chi \approx 1.25$ from Eq. (11), which is very close to our experimental result.

The simplest rationalization of the reduced value of the speed ratio χ is related to the finite size of the RBCs. The size of the vessels is, on the average, only twice the size of the red blood cells ($\delta_{\mathrm{RBC}} \approx 5$ μm): the red blood cells are, therefore, most of the time rolling over the epithelium along the vessel. The minimum distance from the epithelium at which we can measure the flow speed is then only half the red blood cell size, $\approx \delta_{\mathrm{RBC}}/2$. For a circular capillary of diameter d_V in Poiseuille regime, the speed profile is $V(r) - V_{\max}[1 - (2r/d_V)^2]$ and the minimum speed value measurable due to the finite size of the red blood cells should then be $V_{\min} = V_{\max}\{1 - [(d_V - \delta_{\mathrm{RBC}})/d_V]^2\}$. For the present case, these estimates lead to $\chi \approx 1.6$, a value that, though not so low as the one found experimentally, is much less than the one corresponding to pure Poiseuille flow in no-slip boundary conditions. In larger capillaries, additional hydrodynamic effects (reduced effective viscosity close to the vessel walls) can partially contribute to the reduction of χ.[37,48,51]

In the above measurements, we exploited dual line scanning coupled with CCF computation on the EM-CCD frames. This technique can also be used to simultaneously monitor flows in closely running vessels. Such a situation is found in zebrafish close to the capillary bed (5% from tail, see Fig. 6, image) at the transition between artery and vein in the embryo tail. We have scanned two parallel lines (40 μm apart) close to the zebrafish tail capillary bed and derived the drift velocity from the analysis of the CCFs (Fig. 8). We also notice here the presence of a systolic and a diastolic phase in the vein CCFs.

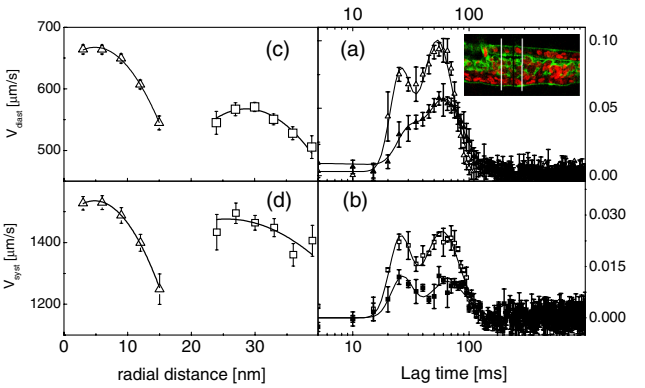

Fig. 8 CCFs acquired simultaneously on zebrafish at heart-tail 5% distance from the tail (see zebrafish embryo picture in Fig. 6). (a) CCFs measured in artery at two radial positions corresponding to 3 (open triangles) and 12 μm (filled triangles) along the scanning line in (c) and (d) (open triangles). (b) CCFs measured in vein at two radial positions corresponding to 24 (open squares) and 33 μm (filled squares) in (c) and (d) (open squares). In (a) and (b), the solid lines are best fit of the CCFs to Eq. (5) with two drift components. (c) and (d) report the best fit drift speed, obtained from the analysis of the CCFs, as a function of the position across the vessel. (c) Diastolic component (open triangle, artery; open squares, vein). (d) Systolic component (open triangle, artery; open squares, vein). The solid lines are the best fit to the parabolic function $V(r) = V(r_0) - [V(r_0) - V(r_0 \pm d_V/2)][2(r - r_0)/d_V]^2$. The image shows a blow up of a section of a zebrafish embryo close to the tail (5%, artery above, vein below). Green and red colors indicate the epithelium emission (GFP) and the red blood cells (dsRed). The white horizontal lines represent the two lines scanned during the fluorescence correlation spectroscopy measurements.

From the speed profiles, we can also derive in this position the relevant parameters such as the velocity ratio, $\chi \approx 1.18 \pm 0.03$ for the artery and $\chi \approx 1.12 \pm 0.05$ for the vein, and the strain rate that is larger in the artery, both for the systole and the diastole phases, $\gamma = 19 \pm 6\ \mathrm{s}^{-1}$ (diastole) and $\gamma = 40 \pm 15\ \mathrm{s}^{-1}$ (systole), than in the vein, $\gamma = 11 \pm 5\ \mathrm{s}^{-1}$ (diastole) and $\gamma = 12 \pm 9\ \mathrm{s}^{-1}$ (systole).

5 Conclusions

The two-spots excitation mode coupled to a sensitive wide-field EM-CCD detection allows us to investigate flows in *in vitro* experiments (microcapillaries) and in *in vivo* studies, such as the measurement of blood flow speed in blood vessels of living embryos of zebrafish. This setup also allows simultaneous acquisition of wide-field transmission images. The novelty here lies in the use of pixelated highly sensitive detectors (EM-CCD) to obtain wide-field information of the motion of the sample based on the parallel detection of extended illumination patterns. The flexibility of the illumination pattern that we shine on the sample is obtained here by coupling an interferometer, used to split the laser beam, to a home-made large-aperture scanning system. The system described allows to derive detailed information on the complex fluido-dynamic systems, obtaining a real-time mapping of the speed field, as demonstrated here in the speed profile measured on a large fraction of the microcapillary section and in zebrafish microvessels *in vivo*. The sensitivity in the measurement of the drift speed allows us to

discriminate systolic and diastolic phases in flows in zebrafish arteries at different distances from the heart. The use of diffractive active systems combined to two-photon excitation would allow, in the future, mapping dynamic processes with high three-dimensional spatial resolution (1 to 2 μm) through biological networks. Possible applications could be the blood flow map in the hepatic microcirculation or the spatiotemporal organization of neurons' network. In fact, by means of spatial light modulators, arbitrary three-dimensional excitation light patterns can be shone on the sample whose dynamics can be followed at millisecond time resolution with CMOS or EM-CCD cameras.[52]

Acknowledgments

This work has been partially funded by the Progetto regionale Accordo Quadro 2005 to G.C. and by the MIUR 2008JZ4MLB PRIN project to M.C. We are also grateful to Dr. Andrea Bassi (politecnico di Milano, Milano) for useful suggestions for the preparation of zebrafish embryos for *in vivo* imaging, to Dr. Carlo Emanuele Villa for the essential help in constructing the reflective scanning head, and to Dr. Chiara Maugeri for help in measurements on zebrafish embryos.

References

1. S. A. Kim, K. G. Heinze, and P. Schwille, "Fluorescence correlation spectroscopy in living cells," *Nat. Meth.* **4**(11), 963–973 (2007).
2. M. A. Digman and E. Gratton, "Lessons in fluctuations correlation spectroscopy," *Ann. Rev. Phys. Chem.* **62**, 645–668 (2011).
3. D. Magde, W. W. Webb, and E. Elson, "Thermodynamic fluctuations in a reacting system–measurement by fluorescence correlation spectroscopy," *Phys. Rev. Lett.* **29**(11), 705–708 (1972).
4. M. Ehrenberg and R. Rigler, "Rotational Brownian-motion and fluorescence intensity fluctuations," *Chem. Phys.* **4**(3), 390–401 (1974).
5. R. Rigler, "FCS and single molecule spectroscopy," Chapter 4 in *Single Molecule Spectroscopy in Chemistry, Physics and Biology*, A. Gräslund, R. Rigler, and J. Widengren, Eds., Vol. 96, pp. 77–103, Springer Verlag, Berlin (2010).
6. P. C. Brister et al., "Fluorescence correlation spectroscopy for flow rate imaging and monitoring–optimization, limitations and artifacts," *Lab Chip* **5**(7), 785–791 (2005).
7. D. Magde, W. W. Webb, and E. L. Elson, "Fluorescence correlation spectroscopy 3. Uniform translation and laminar-flow," *Biopolymers* **17**(2), 361–376 (1978).
8. M. Gösch et al., "Hydrodynamic flow profiling in microchannel structures by single molecule fluorescence correlation spectroscopy," *Anal. Chem.* **72**(14), 3260–3265 (2000).
9. K. K. Kuricheti, V. Buschmann, and K. D. Weston, "Application of fluorescence correlation spectroscopy for velocity imaging in microfluidic devices," *Appl. Spec.* **58**(10), 1180–1186 (2004).
10. K. Liu et al., "Mapping vortex-like hydrodynamic flow in microfluidic networks using fluorescence correlation spectroscopy," *Analytica Chimica Acta* **651**(1), 85–90 (2009).
11. X. Shi et al., "Probing events with single molecule sensitivity in Zebrafish and Drosophila embryos by fluorescence correlation spectroscopy," *Develop. Dyn.* **238**(12), 3156–3167 (2009).
12. K. Brinkmeier, J. S. Doerre, and M. Eigen, "Two-beam cross-correlation: a method to characterize transport phenomena in micrometer-sized structures," *Anal. Chem.* **71**(3), 609–616 (1999).
13. P. S. Dittrich and P. Schwille, "Spatial two-photon fluorescence cross-correlation spectroscopy for controlling molecular transport in microfluidic structures," *Anal. Chem.* **74**(17), 4472–4479 (2002).
14. T. Dertinger et al., "Two-focus fluorescence correlation spectroscopy: a new tool for accurate and absolute diffusion measurements," *Chem. Phys. Chem.* **8**(3), 433–443 (2007).
15. C. B. Mueller et al., "Precise measurement of diffusion by multi-color dual-focus fluorescence correlation spectroscopy," *Eur. Phys. Lett.* **83**(4), p1–p5 (2008).
16. T. J. Arbour and J. Enderlein, "Application of dual-focus fluorescence correlation spectroscopy to microfluidic flow-velocity measurement," *Lab Chip* **10**(10), 1286–1292 (2010).
17. D. J. Grunwald and J. S. Eisen, "Headwaters of the zebrafish–emergence of a new model vertebrate," *Nat. Rev. Genet.* **3**(9), 717–724 (2002).
18. M. C. Mione and N. S. Trede, "The zebrafish as a model for cancer," *Dis. Model Mech.* **3**(9–10), 517–523 (2010).
19. E. L. Elson and D. Magde, "Fluorescence correlation spectroscopy .1. Conceptual basis and theory," *Biopolymers* **13**(1), 1–27 (1974).
20. J. Enderlein and W. P. Ambrose, "Optical collection efficiency function in single-molecule detection experiments," *Appl. Opt.* **36**(22), 5298–5302 (1997).
21. A. Diaspro, G. Chirico, and M. Collini, "Applications in two-photon excitation microscopy," *Quart. Rev. Biophys.* **38**(2), 97–166 (2005).
22. J. B. Freund et al., "Fluid flows and forces in development: functions, features and biophysical principles," *Development* **139**(7), 1229–1245 (2012).
23. B. Vollmar, S. Siegmund, and M. D. Menger, "An intravital fluorescence microscopic study of hepatic microvascular and cellular derangements in developing cirrhosis in rats," *Hepatol.* **27**(6), 1544–1553 (1998).
24. M. Thiriet and K. H. Parker, "Physiology and pathology of the cardiovascular system: a physical perspective," Chapter 1 in *Cardiovascular Mathematics: Modeling and Simulation of the Circulatory System*, L. Formaggia, A. Quarteroni, and A. Veneziani, Eds., pp. 1–46, Springer Verlag, Italia (2009).
25. Y. Blum et al., "Complex cell rearrangements during intersegmental vessel sprouting and vessel fusion in the zebrafish embryo," *Dev. Biol.* **316**(2), 312–322 (2008).
26. C.-Y. Chen et al., "Analysis of early embryonic great-vessel microcirculation in zebrafish using high-speed confocal mu PIV," *Biorheol.* **48**(5–6), 305–321 (2011).
27. P. Pallavicini et al., "Synthesis of branched Au nanoparticles with tunable near-infrared LSPR using a zwitterionic surfactant," *Chem. Commun.* **47**(4), 1315–1317 (2011).
28. N. D. Lawson and B. M. Weinstein, "In vivo imaging of embryonic vascular development using transgenic zebrafish," *Dev. Biol.* **248**(2), 307–318 (2002).
29. M. A. Akimenko et al., "Differential induction Of 4 Msx Homeobox genes during fin development and regeneration in Zebrafish," *Development* **121**(2), 347–357 (1995).
30. A. Bassi et al., "In vivo label-free three-dimensional imaging of zebrafish vasculature with optical projection tomography," *J. Biomed. Opt.* **16**(10), 100502 (2011).
31. L. Sironi et al., "Gold branched nanoparticles for cellular treatments," *J. Chem. Phys. C* **116**(34), 18407–18418 (2012).
32. A. J. García-Sáez and P. Schwille, "Fluorescence correlation spectroscopy for the study of membrane dynamics and protein/lipid interactions," *Methods* **46**(2), 116–122 (2008).
33. S. K. Wilson and B. R. Duffy, "A rivulet of perfectly wetting fluid draining steadily down a slowly varying substrate," *IMA J. Appl. Math.* **70**(2), 293–322 (2005).
34. Y. Kuo and R. I. Tanner, "Laminar Newtonian flow in open channels with surface-tension," *Int. J. Mech. Sci.* **14**(12), 861–873 (1972).
35. H. Bruus, *Theoretical Microfluidics*, pp. 48–51, 123–136, Oxford University Press, United Kingdom (2008).
36. V. T. Turrito and H. R. Baumgartner, "Platelet interaction with subendotheliumin flowing rabbit blood: effect of blood shear rate," *Microvasc. Res.* **17**(1), 38–54 (1979).
37. G. J. Tangelder et al., "Wall shear rate in arterioles in vivo: least estimates from platelet velocity profiles," *Am. J. Physiol.* **254**(6), H1059–H1064 (1988).
38. X. Pan et al., "Characterization of flow direction in microchannels and zebrafish blood vessels by scanning fluorescence correlation spectroscopy," *J. Biomed. Opt.* **12**(1), 014034 (2007).
39. M. Oishi et al., "Continuous and simultaneous measurement of the tank-treading motion of red blood cells and the surrounding flow using translational confocal micro-particle image velocimetry (micro-PIV) with sub-micron resolution," *Meas. Sci. Techn.* **23**(3), 035301 (2012).
40. P. Vennemann et al., "In vivo micro particle image velocimetry measurements of blood-plasma in the embryonic avian heart," *J. Biomech.* **39**(7), 1191–1200 (2006).

41. M. L. Smith et al., "Near-wall mu-PIV reveals a hydrodynamically relevant endothelial surface layer in venules in vivo," *Biophys. J.* **85**(1), 637–645 (2003).
42. H. Cheng et al., "Modified laser speckle imaging method with improved spatial resolution," *J. Biomed. Opt.* **8**(3), 559–564 (2003).
43. W. Wang et al., "Optical trapping and fluorescence detection in laminar flow streams," *Appl. Phys. Lett.* **67**(8), 1057–1059 (1995).
44. B. Manz et al., "NMR imaging of the time evolution of electroosmotic flow in a capillary," *J. Phys. Chem.* **99**(29), 11297–11301 (1995).
45. L. Fieramonti et al., "Quantitative measurement of blood velocity in zebrafish with optical vector field tomography," *J. Biophotonics* (2013) [Epub ahead of print].
46. J. R. Hove et al., "Intracardiac fluid forces are an essential epigenetic factor for embryonic cardiogenesis," *Nature* **421**(6919), 172–177 (2003).
47. R. S. Reneman, T. Arts, and A. P. G. Hoeks, "Wall shear stress—an important determinant of endothelial cell function and structure—in the arterial system in vivo discrepancies with theory," *J. Vasc. Res.* **43**(3), 251–269 (2006).
48. Z. Zhong et al., "Noninvasive measurements and analysis of blood velocity profiles in human retinal vessels," *Invest. Ophthalmol. Vis. Sci.* **52**(7), 4151–4157 (2011).
49. P. Gaehtgens, H. J. Meiselman, and H. Wayland, "Velocity profiles of human blood at normal and reduced hematocrit in glass tubes up to 130 micrometer diameter," *Microvasc. Res.* **2**(1), 13–23 (1970).
50. R. T. Yen and Y. C. Fung, "Effect of velocity distribution on red-cell distribution in capillary blood-vessels," *Am. J. Physiol.* **235**(2), H251–H257 (1978).
51. T. W. Secomb, "Mechanics of blood flow in the microcirculation," *Symp. Soc. Exp. Biol.* **49**(1), 305–321 (1995).
52. D. Gandolfi et al., "The spatiotemporal organization of cerebellar network activity resolved by two-photon imaging of multiple single neurons," *Front. Cell. Neurosci.* **8**, 92 (2014).

Paolo Pozzi is a PhD student in physics at the biophotonics group at the Università degli Studi di Milano-Bicocca. His main scientific interest is in the development of optical microscopy techniques combining the use of structured multiphoton excitation and pixelated detectors, for the acquisition of high temporal resolution signals in multiple positions on the sample.

Laura Sironi received her PhD in physics in 2011 from the Università deglli Studi di Milano-Bicocca and is currently a research fellow in applied physics in the Physics Department of this university. Her research interests are in *in vivo* nonlinear microscopy and image correlation spectroscopy for immunology.

Laura D'Alfonso received her PhD in physics in 2000 from the Università degli Studi di Milano and is a research fellow in applied physics at the Physics Department of the Università degli Studi di Milano-Bicocca. Her research activity is in molecular biophysics and dynamic properties of proteins.

Margaux Bouzin is a PhD student in physics at the Università degli Studi di Milano-Bicocca and working on the development of correlative analysis of raster scanning images for the measurement of dynamic parameters in biological systems.

Maddalena Collini received her PhD in physics in 1992 and is currently a professor of applied physics at the Università degli studi di Milano-Bicocca. Her interests are in optical superresolution microscopy and image correlation applied to biotechnology.

Giuseppe Chirico received his PhD in physics in 1990 from the Università degli Studi di Milano and is currently a professor of applied physics at Università degli studi di Milano-Bicocca. His interests are in optical microscopy and correlative spectroscopy for biophysics.

Piersandro Pallavicini received his PhD in chemistry from the Scuola Normale Superiore di Pisa in 1990. He is currently a professor of chemistry at the Università degli studi di Pavia. His research interests and expertise are in coordination chemistry and metal nanoparticle synthesis and application to sensing, biology, and medicine.

Franco Cotelli obtained his Laurea degree in biological sciences from the University of Milano. He is a professor of developmental biology at the University of Milano and PI of the Zebrafish Laboratory at the Biosciences Department. Since the 1990s he has focused on zebrafish to study vertebrate development and genes involved in human diseases (nervous, cardiovascular, and hematopoietic system).

Efrem A. Foglia obtained his PhD in animal biology from Università degli Studi di Milano in 2012 and is currently a research fellow at the Università degli Studi di Milano, Department of Bioscience. Currently, he works on developmental biology, vasculogenesis, angiogenesis, and vascular diseases using zebrafish (Danio rerio) as a model system.